



Title: Phase relations in the system $\text{MgSiO}_3\text{-Al}_2\text{O}_3$ up to 2300 K at lower mantle pressures
Author: Zhaodong Liu, Masayuki Nishi, Takayuki Ishii, Hongzhan Fei, Nobuyoshi Miyajima, Tiziana Boffa Ballaran, Hiroaki Ohfuji, Takeshi Sakai, Lin Wang, Svyatoslav Shcheka, Takeshi Arimoto, Yoshinori Tange, Yuji Higo, Tetsuo Irifune, Tomoo Katsura
Publication: Journal of Geophysical Research: Solid Earth
Publisher: AGU Wiley
Date: 09 October 2017

This is the peer reviewed version of the following article: [Liu, Z., Nishi, M., Ishii, T., Fei, H., Miyajima, N., Ballaran, T. B., ... Katsura, T. (2017). Phase relations in the system $\text{MgSiO}_3\text{-Al}_2\text{O}_3$ up to 2300 K at lower mantle pressures. Journal of Geophysical Research: Solid Earth, 122, 7775–7788], which has been published in final form at <https://doi.org/10.1002/2017JB014579>. This article may be used for non-commercial purposes in accordance with Wiley Terms and Conditions for Use of Self-Archived Versions.

1 **Phase relations in the system MgSiO₃–Al₂O₃ up to 2300 K at lower-mantle**
2 **pressures**

3 Zhaodong Liu ^{1,2*}, Masayuki Nishi ², Takayuki Ishii ¹, Hongzhan Fei ¹, Nobuyoshi Miyajima ¹,
4 Tiziana Boffa Ballaran ¹, Hiroaki Ohfuji ², Takeshi Sakai ², Lin Wang ¹, Svyatoslav Shcheka ¹,
5 Takeshi Arimoto ², Yoshinori Tange ³, Yuji Higo ³, Tetsuo Irifune ², Tomoo Katsura ¹

6 ¹Bayerisches Geoinstitut, University of Bayreuth, 95440 Bayreuth, Germany

7 ²Geodynamics Research Center (GRC), Ehime University

8 ³Spring-8, Japan Synchrotron Radiation Institute

9

10 * Corresponding author: Zhaodong Liu (bt303897@uni-bayreuth.de)

11 Bayerisches Geoinstitut, University of Bayreuth, 95440 Bayreuth, Germany

12

13 **Key Points:**

- 14 • Phase relations in the system MgSiO₃-Al₂O₃ were determined at temperatures up to 2300
15 K and pressures up to 45 GPa.
- 16 • The solubility of Al₂O₃ in bridgmanite and that of MgSiO₃ in corundum increase with
17 increasing temperature.
- 18 • The Al₂O₃ cannot be fully accommodated in the coldest parts of subducted slabs in the
19 shallow part of the lower mantle.

20

21

22

23

24 Abstract

25 Phase relations in the system $\text{MgSiO}_3\text{--Al}_2\text{O}_3$ were investigated at pressures of 27–45 GPa and
26 temperatures of 1700, 2000 and 2300 K using sintered diamond and tungsten carbide anvils in a
27 multi-anvil apparatus. The bulk compositions in the $\text{MgSiO}_3\text{--Al}_2\text{O}_3$ binary system crystallize a
28 phase assemblage of pyrope and corundum at pressures below 27 GPa and an assemblage of
29 bridgmanite and corundum at pressures above 27 GPa regardless of temperatures. The solubility
30 of Al_2O_3 in bridgmanite and that of MgSiO_3 in corundum increase significantly with increasing
31 temperature. The solubility of Al_2O_3 in bridgmanite increases from 6.7 mol% at 1700 K to 21.8
32 mol% at 2500 K under a constant pressure of 27 GPa. Bridgmanite becomes more aluminous with
33 increasing pressure from 27 to 45 GPa at a given temperature. The MgSiO_3 content in corundum
34 increases with increasing pressure at pressure lower than 27 GPa, while it decrease at pressure
35 higher than 27 GPa. Our results suggest that bridgmanite can incorporate a considerably higher
36 Al_2O_3 content than that of the pyrope composition (25 mol% Al_2O_3). The present study further
37 suggests that the entire Al_2O_3 component is accommodated into bridgmanite in the pyrolite lower
38 mantle. However, Al_2O_3 cannot be fully accommodated into bridgmanite in the coldest parts of
39 subducted slabs in the shallow part of the lower mantle, and therefore additional phases such as
40 MgAl_2O_4 with calcium ferrite-type structure are necessary to host the excess Al_2O_3 .

41 Keywords: phase relations, bridgmanite, Al_2O_3 , subducted slabs, lower mantle

42

43

44

45 1. Introduction

46 Al_2O_3 is the fourth most abundant component in the Earth's mantle [Ringwood, 1975;
47 MacDough and Sun, 1995]. It has been put in the spotlight because of its importance for
48 understanding the mineralogy of the Earth's mantle. Al_2O_3 makes up about 4 wt% in the pyrolite
49 mantle [Sun, 1982] and as much as about 16 wt% in the mid-oceanic ridge basalt (MORB) layers
50 in subducted slabs [Green *et al.*, 1979]. From the upper mantle to the transition zone, Al_2O_3 is
51 primarily accommodated into garnet solid solutions in both pyrolite and MORB compositions
52 [Ringwood, 1967; Irifune, 1987]. Under lower-mantle conditions, the entire Al_2O_3 can be
53 incorporated into bridgmanite, the most abundant mineral in the Earth's mantle, in the pyrolite
54 composition [Irifune, 1994]. On the other hand, bridgmanite cannot accommodate all Al_2O_3 in the
55 MORB composition, and some Al_2O_3 may be accommodated in several Al-rich phases in addition
56 to bridgmanite. [e.g., Irifune and Ringwood, 1993; Ono *et al.*, 2001; Hirose and Fei, 2002].
57 Moreover, the incorporation of Al_2O_3 can greatly change the crystal chemistry of bridgmanite [e.g.,
58 McCammon, 1997]; and thereby significantly affect its physical properties such as elastic
59 properties [Zhang and Weidner, 1999; Brodholt, 2000] and electrical conductivity [Xu *et al.*,
60 1998]. Therefore, knowledge about the Al_2O_3 effects on the crystal chemistry of bridgmanite is of
61 great significance in mineral physics and geophysics, and is seminal for understanding the
62 mineralogy of the lower mantle.

63 To understand the Al_2O_3 solubility in bridgmanite better, phase relations in the system
64 MgSiO_3 – Al_2O_3 have been studied extensively at pressure below 27 GPa [Irifune *et al.*, 1996; Kubo
65 and Akaogi, 2000; Hirose *et al.*, 2001; Akaogi *et al.*, 2002]. These studies suggested that
66 bridgmanite coexists with corundum in this system at pressures above 26 GPa. Recently, Liu *et al.*
67 [2016] demonstrated that the Al_2O_3 solubility in bridgmanite increases from 12 to 29 mol% with

68 increasing pressure from 27 to 52 GPa at a temperature of 2000 K. The pressure dependence at a
69 given temperature, therefore, is now clear, however, the temperature dependence of the Al₂O₃
70 incorporation in bridgmanite is still poorly constrained. [Irifune *et al.* \[1996\]](#) suggested that it
71 increases from 11 mol% at 1760 K to 17 mol% at 2030 K at a pressure of 27 GPa, whereas [Kubo
72 and Akaogi \[2000\]](#) experiments showed an increase from 8 to 13 mol% with increasing
73 temperature from 1670 to 2170 K at almost the same pressure. Therefore, these two studies
74 disagree significantly. Moreover, these studies were conducted only at the lowest pressure
75 conditions for the bridgmanite and corundum coexistence, and no studies have reported the
76 temperature effect on the Al₂O₃ solubility in bridgmanite at higher pressures. Temperatures in the
77 subducted slabs should be significantly lower than in the surrounding mantle, but should approach
78 that of the surrounding mantle due to thermal equilibration [e.g., [Ringwood, 1991](#); [Irifune and
79 Ringwood, 1993](#); [Kirby *et al.*, 1996](#)]. Consequently, the temperature effects are vital to constrain
80 the slab dynamics. Nevertheless, our limited knowledge about the temperature dependence of the
81 Al₂O₃ solubility in bridgmanite prevents us from understanding the mineralogy in the deep
82 subducted slabs.

83 The reason for our limited knowledge about the temperature dependence of the Al₂O₃ solubility
84 in bridgmanite is the technical difficulty in high-pressure and high-temperature experiments.
85 Although use of the multi-anvil technique is desired for the determination of phase transitions in
86 multiple-component systems, the pressure ranges of conventional multi-anvil presses are restricted
87 to 27 GPa at high temperatures due to the limited hardness of tungsten carbide (WC) anvils.
88 However, recent development of high-pressure and high-temperature technology using sintered-
89 diamond (SD) anvils in conjunction with *in situ* synchrotron X-ray diffraction observations allows
90 generation of accurate pressures up to 50 GPa routinely at high temperature [[Tange *et al.*, 2008](#);

91 [Liu et al., 2016](#)]. By utilizing these techniques, we have investigated phase relations in the system
92 $\text{MgSiO}_3\text{--Al}_2\text{O}_3$ at temperatures up to 2300 K and pressures up to 45 GPa. Based on our new results,
93 the Al_2O_3 solubility in bridgmanite and the host phases of Al_2O_3 in the lower mantle are discussed.

94

95 2. Experimental methods

96 A fine-grained oxide mixture of composition $\text{En}_{50}\text{Cor}_{50}$ (En: MgSiO_3 , Cor: Al_2O_3 ; the number
97 represents mol%, oxide grain size: 50 nm) and $\text{En}_{75}\text{Cor}_{25}$ glass (pyrope composition, hereafter
98 denoted as pyropic glass) along the $\text{MgSiO}_3\text{--Al}_2\text{O}_3$ join are used as starting materials. Detailed
99 chemical compositions of those two starting materials were reported in [Liu et al. \[2016\]](#) and also
100 examined using an electron probe microanalyzer in the present study (see Table S1 in supporting
101 information). The starting materials were put into graphite or platinum capsules and then heated at
102 800 K for one hour to purge water, and finally put into the cell assembly for the high-pressure and
103 high-temperature experiments.

104 *In situ* X-ray diffraction (XRD) experiments were performed at pressures of 32–49 GPa at
105 temperatures of 1700 and 2000 K using SD anvils with 1.5 mm truncation as second-stage anvils
106 in a DIA-type multi-anvil apparatus at the synchrotron radiation facility, SPring-8 (SPEED-*Mk.*
107 *II*). The experimental facility for *in situ* XRD measurements was described by [Katsura et al.](#)
108 [\[2004\]](#), and the ultrahigh pressure cell assembly was identical to that of [Tange et al. \[2009\]](#), as
109 also shown in **Figure 1**. Pressures were determined based on the $P\text{--}V\text{--}T$ equation of state of Au
110 proposed by [Tsuchiya \[2003\]](#). General relations between the generated pressure and the press load
111 at temperatures of 300, 1700 and 2000 K are shown in **Figure 2a**. Uncertainties in pressure
112 determination in these *in situ* experiments are approximately ± 0.2 GPa. Sample temperatures were

113 measured with a $W_{97}Re_3$ – $W_{75}Re_{25}$ thermocouple, whose hot junction was placed on the bottom of
114 the sample capsule. The sample was compressed to the target pressure and then heated at the target
115 temperature for 3–5 hours. *In situ* XRD patterns were collected for 3–5 hours at the target pressure
116 and temperature. Then, the run was quenched by turning off the electronic power, and the pressure
117 was released slowly over several hours. Finally, *in situ* XRD patterns of the quenched samples
118 were collected under ambient conditions for one hour.

119 We also conducted high-pressure quench experiments at the Bayerisches Geoinstitut,
120 University of Bayreuth, Germany. Runs at pressures below 25 GPa were conducted using WC
121 anvils with a 10.0 mm octahedral pressure medium and 4.0 mm anvil truncation in a 12-MN multi-
122 anvil press with a split-sphere guide block (Sumitomo 1200-ton) [Keppler and Frost, 2005]. One
123 run conducted at a pressure of 35 GPa and a temperature of 2300 K was also performed using WC
124 anvils with 1.5 mm truncation with this press. This pressure at 2300 K was estimated from the FeO
125 content in bridgmanite [Tange *et al.*, 2009], in equilibrium with magnesiowüstite and stishovite,
126 using synthetic $(Mg_{0.7}Fe_{0.3})SiO_3$ pyroxene as a starting material (see Text S1 and Figure S1 in
127 supporting information for pressure calibration details). Runs at pressures above 25 GPa were
128 performed using a 7 and 5.7 mm pressure medium and 3 and 1.5 mm truncation, respectively, in a
129 15-MN press with a DIA-type guide block system (IRIS-15) [Ishii *et al.*, 2016]. **Figure 2b** shows
130 the relationships between pressures and press loads at temperatures of 1700 and 2000 K for IRIS-
131 15, which were calibrated using decomposition of pyrope into aluminous bridgmanite and
132 corundum [Hirose *et al.*, 2001] and the Al_2O_3 solubility in bridgmanite [Liu *et al.*, 2016]. Pressure
133 uncertainties of these quench experiments were on the order of ± 0.5 GPa.

134 Recovered samples were mounted in epoxy resin, ground to expose the central portion, and
135 then polished using 0.25 μm diamond paste. Phases present in the quench runs were identified

136 using a micro-focused X-ray diffractometer (XRD, Bruker, D8 DISCOVER) equipped with a two-
137 dimensional solid state detector (VANTEC500) and a micro-focus source ($I\mu S$) with $Co-K\alpha$
138 radiation operated at 40 kV and 500 μA . The X-ray beams were focused to 50 μm using a IFG
139 polycapillary X-ray mini-lens. Textural observation was performed using a LEO1530 scanning
140 electron microscope (SEM) operating at an acceleration voltage of 15–20 kV and a beam current
141 of 10 nA. Chemical compositions of each phase present in the quench runs were determined using
142 a JEOL JXA-8200 electron probe microanalyzer (EPMA) operating at acceleration voltages of 10
143 or 15 kV and a beam current of 5 nA with standards of enstatite for Mg and Si, and pyrope for Al.

144 **3. Results**

145 Experimental conditions and phases present in the recovered samples are listed in **Table 1**. At
146 pressures below 25 GPa under temperatures of 1700 and 2300 K, the starting material of $En_{50}Cor_{50}$
147 transforms into pyrope and corundum (see Figure S2 in supporting information), and these
148 corundum can contain significant amounts of the $MgSiO_3$ component (see Table S2 in supporting
149 information). The $MgSiO_3$ solubility in corundum increases with increasing pressure and
150 temperature, e.g., 7.9 ± 0.4 mol% at 20 GPa to 12.6 ± 0.6 mol% at 25 GPa under a temperature of
151 1700 K and 12.6 ± 0.6 mol% at 1700 K to 26.7 ± 0.7 mol% at 2300 K under a pressure of 25 GPa.

152 **Figure 3a** shows representative back-scattered electron images of the quenched samples for
153 $En_{50}Cor_{50}$ oxide mixture and pyropic glass at a pressure of 27 GPa and at temperatures of 1700
154 and 2500 K, respectively. The corresponding XRD profiles in **Figure 3b** and Figure S2 (see
155 supporting information) of these run products are consistent with the presence of a mixture of
156 bridgmanite and corundum. As shown in **Table 2**, the chemical compositions of phases in the

157 recovered samples using these two different starting materials are identical within analytical
158 uncertainties, implying that chemical equilibrium was achieved under these conditions.

159 **Figure 4** illustrates the solubility of Al₂O₃ in bridgmanite and that of MgSiO₃ in corundum,
160 respectively, as a function of temperatures at a constant pressure of 27 GPa as determined in the
161 present and previous studies [Irifune *et al.*, 1996; Kubo and Akaogi, 2000; Akaogi *et al.*, 2002;
162 Liu *et al.*, 2016]. The Al₂O₃ solubility in bridgmanite apparently increases linearly with
163 temperature (**Figure 4a**), and this tendency is similar to that for FeO in bridgmanite reported by
164 Fei *et al.* [1996]. In the present study, the Al₂O₃ solubility in bridgmanite reaches 21.7 ± 0.6 mol%
165 at 2500 K. The best fit of all the experimental data to a linear function yields the relation of
166 $X_{\text{Al}_2\text{O}_3} = -0.19 (2) + 1.60 (1) \cdot 10^{-5} \cdot T$, where $X_{\text{Al}_2\text{O}_3}$ is the Al₂O₃ solubility in mole percent
167 in bridgmanite at a pressure of 27 GPa, T is the temperature in Kelvin and the number in
168 parentheses represents standard deviations for the last digit. This equation suggests that
169 bridgmanite with a pyrope composition, i.e., with 25 mol% Al₂O₃, could form at a temperature of
170 approximately 2750 K at this pressure. **Figure 4b** demonstrates that the MgSiO₃ solubility in
171 corundum also increases with increasing temperature at 27 GPa, and reaches as much as 38.0 ±
172 0.5 mol% at 2500 K in the present study. The values for corundum reported by Irifune *et al.* [1996]
173 and Kubo and Akaogi [2000] are, however, larger than those in the present study at given the same
174 temperature. One possible reason for this discrepancy may be related to the low resolution of the
175 EPMA due to the small grain sizes of corundum and bridgmanite obtained in earlier studies. The
176 grain size of phases in the runs at 27 GPa in our study is considerably larger than 3 μm in **Figure**
177 **3**, the composition is thus accurate due to the grain size is larger than the resolution of the EPMA.

178 **Figure 5** shows selected back-scattered electron images of the quenched samples for the
179 En₅₀Cor₅₀ oxide mixture and pyrope glass at pressures higher than 27 GPa. Aluminous

180 bridgmanite, corundum, and Au pressure markers are found in these *in situ* runs. **Figure 6a** shows
181 *in situ* synchrotron XRD patterns for En₅₀Cor₅₀ under 31.9–48.5 GPa at 1700 K. In all XRD
182 patterns, the major peaks are assigned to bridgmanite, corundum, and Au, while the other minor
183 ones can be assigned to stishovite, surrounding diamond capsules, and MgO disks. For the product
184 recovered from the run at 48.5 GPa and 1700 K for two hours, the element mapping by means of
185 analytical transmission electron microscopy (ATEM) reported in Figure S3 further confirms that
186 bridgmanite, corundum and trace amount of stishovite coexist in this sample. However, the TEM
187 mapping combined with energy dispersive X-ray spectroscopy (EDXS) suggest the compositions
188 of these phases are not homogeneous, which may be caused by the unreached chemical equilibrium
189 due to the short heating time as a result of the instability of the heater in this run (Text S2). **Figure**
190 **6b** shows the XRD pattern of the S6615 run. It is found that perovskite with a LiNbO₃ structure
191 with a rhombohedral symmetry coexists with corundum at 35 GPa and 2300 K. EPMA analysis
192 on this LiNbO₃ structure demonstrate that it contains 27.3 ± 0.3 mol% of Al₂O₃. Its lattice
193 parameters ($a = b = 4.849$ (1); $c = 12.712$ (10)) are slightly higher than those ($a = b = 4.783$ (2); c
194 $= 12.680$ (11)) for the same phase with the pyrope composition obtained by Liu *et al.* [2016],
195 which can be explained by a higher Al₂O₃ content in the present study than that of the latter study.
196 The present result further confirms that bridgmanite with the Al₂O₃ content higher than 25 mol%
197 would transform into the LiNbO₃ structure upon releasing pressure, which is consistent with the
198 result of earlier works [Funamori *et al.*, 1997; Miyajima *et al.*, 1999; Liu *et al.*, 2016; Ishii *et al.*,
199 2017]. However, Liu *et al.* [2016] also found that the bridgmanite phase containing 29.5 mol%
200 exists in the M1677 run, and this difference may be caused by the effect of nanoscale grain size
201 with a higher surface energy as suggested by Liu *et al.* [2016].

202 Two experiments were performed using the pyropic glass as the starting material at pressures
203 of 42.3 and 44.5 GPa and at temperatures of 2000 and 1700 K, respectively (**Figure 6c**). *In situ*
204 XRD observations suggest that the phases present in these runs are bridgmanite and corundum. In
205 particular, a trace amount of corundum coexists with bridgmanite at 42.3 GPa and 2000 K, which
206 is also confirmed by the back-scattered electron observations in **Figure 5d**. Composition analysis
207 on several large grains (3 μm) suggests that bridgmanite in this recovered sample contains $21.9 \pm$
208 0.6 mol% Al_2O_3 . These results suggest that bridgmanite with the pyrope composition should form
209 at a slightly higher pressure than 42.3 GPa, providing more convincing evidence that the Al_2O_3
210 solubility exceeds 25 mol% above 45 GPa at 2000 K [Liu *et al.*, 2016]. The composition of
211 bridgmanite in M1677 run (51.8 GPa and 2000 K) in Liu *et al.* [2016] was estimated based on
212 relations between unit-lattice parameters and Al_2O_3 contents. Here, instead, we determined the
213 accurate compositions of the phases in M1677 run by adjusting the EPMA analytical beam-size to
214 1 μm , and found that the Al_2O_3 content in bridgmanite is 29.5 ± 0.7 mol%, in excellent agreement
215 with that (29 ± 5 mol%) estimated from its unit-cell lattice parameters. Therefore, for the sample
216 at 44.5 GPa and 1700 K, since the grain size of this run product is smaller than 1 μm , the Al_2O_3
217 content in bridgmanite has been estimated to be approximately 16 ± 3 mol% from its unit-cell
218 lattice parameters (see Table S3 in supporting information) [Liu *et al.*, 2016].

219 The lattice parameters and molar volume of aluminous bridgmanite and corundum in the
220 present and previous studies [D'Amour *et al.*, 1978; Weng *et al.*, 1981; Ito *et al.*, 1978, 1998;
221 Irifune *et al.*, 1996; Kubo and Akaogi, 2000; Yagi *et al.*, 2004; Walter *et al.*, 2004; Liu *et al.*, 2016]
222 are shown as a function of the Al_2O_3 and MgSiO_3 content, respectively, in **Figure 7**. It is clearly
223 seen that the value of a, b, and c-axis of aluminous bridgmanite increases almost linearly with

224 increasing Al₂O₃ content within analytical uncertainties in **Figure 7a**. A linear function is adapted
225 to the present data and those of [Liu et al. \[2016\]](#), and got the following equations:

$$226 \quad a = 4.777 (\pm 0.001) + 0.014 (\pm 0.007) \times \chi_{\text{Al}_2\text{O}_3}$$

$$227 \quad b = 4.928 (\pm 0.002) + 0.109 (\pm 0.011) \times \chi_{\text{Al}_2\text{O}_3}$$

$$228 \quad c = 6.900 (\pm 0.002) + 0.236 (\pm 0.012) \times \chi_{\text{Al}_2\text{O}_3}$$

229 where $\chi_{\text{Al}_2\text{O}_3}$ represents the mole fraction of the Al₂O₃ in bridgmanite ($0 \leq \chi_{\text{Al}_2\text{O}_3} < 0.30$). These
230 equations agree well with those obtained in [Irifune et al. \[1996\]](#) except that the slope for the change
231 in lattice parameters with the Al₂O₃ content is slightly smaller than that obtained in the latter study.
232 The same equation to corundum produces following results (**Figure 7b**):

$$233 \quad a = b = 4.764 (2) + 0.023(9) \times \chi_{\text{MgSiO}_3}$$

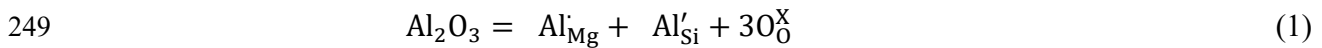
$$234 \quad c = 12.991 (6) + 0.136 (3) \times \chi_{\text{MgSiO}_3}$$

235 where χ_{MgSiO_3} represents the mole fraction of the MgSiO₃ in bridgmanite ($0 \leq \chi_{\text{MgSiO}_3} < 0.4$). The
236 molar volume of bridgmanite increases almost linearly with increasing Al₂O₃ contents (**Figure 7c**),
237 and can be best expressed as $V(x) = 1.35 (8) \cdot x + 24.468 (12)$, where x is the mole
238 fraction of Al₂O₃ ($0 \leq x < 0.3$), and the number in parentheses represents standard deviations for
239 the last digit. It can be also seen in **Figure 7d** that the molar volume of corundum increases slightly
240 with increasing MgSiO₃ contents, expressed as $V(x) = 0.42 (7) \cdot x + 25.64 (1)$, where
241 x is the mole fraction of MgSiO₃ ($0 \leq x < 0.4$). The effect of MgSiO₃ contents on the volume of
242 corundum is significantly smaller than that of Al₂O₃ for bridgmanite.

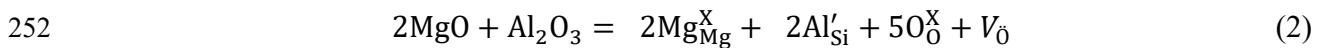
243 **Discussion**

244 4.1 Al substitution mechanism in bridgmanite

245 It is thought that Al is incorporated into the crystal structure of bridgmanite through two
246 types of possible substitution mechanisms [Hirsch and Shankland, 1991; Richmond and Brodholt,
247 1998; Navrotsky *et al.*, 1999, 2003; Andraut *et al.*, 2007]: (1) the charge-coupled substitution:
248 substituting of Mg and Si by Al,



250 (2) the oxygen vacancy substitution: substitution of Al into the Si site and creating an oxygen
251 vacancy,



253 where subscripts indicate the site and superscripts indicate the charge (X) for neutral, (·) for
254 negative charge, (·) for a positive charge (point defect notation from Kröger and Vink [1956]).

255 **Figure 8a** shows the cation ratio between Mg and Si (Mg/Si) as a function of the Al pfu in
256 aluminous bridgmanite in the present study and previous works [Irifune *et al.*, 1996; Kubo and
257 Akaogi, 2000; Liu *et al.*, 2016]. This ratio is mainly along the trend line for the charge-coupled
258 substitution within the analytical uncertainties, while it is far below the trend line of the oxygen
259 vacancy substitution, suggesting the charge-coupled substitution dominates in the aluminous
260 bridgmanite. This result is well consistent with some earlier experimental works on aluminous
261 bridgmanite [Stebbins *et al.*, 2001; Walter *et al.*, 2006]. **Figure 8b** further supports this idea due
262 to the value of Si cation in the bridgmanite is almost along the trend line for the charge-coupled
263 substitution. However, XRD patterns in such as **Figure 3** and **6** demonstrate that trace stishovite

264 coexisted with bridgmanite in some runs, suggesting that trace amounts of the oxygen vacancy
265 substitution may also occurs in the aluminous bridgmanite.

266 **4.2 Phase diagram in the MgSiO₃–Al₂O₃ system**

267 **Figure 9** shows the phase diagram of the garnet-corundum-bridgmanite transition in the
268 system MgSiO₃–Al₂O₃ at pressures of 20–45 GPa and at temperatures of 1700, 2000 and 2300 K.
269 The pressure of the disproportionation of pyrope at various temperatures is estimated from the runs
270 at 1700 and 2000 K in **Figure 2b** together with the study by [Hirose *et al.* \[2001\]](#). At pressures
271 lower than 25 GPa at these three temperatures, En₅₀Cor₅₀ crystallizes an assemblage of pyrope
272 plus corundum. Depending on temperatures, pyrope would decompose into bridgmanite and
273 corundum at 25.5–27 GPa. At a pressure of 27 GPa at these temperatures, the two-phase field of
274 bridgmanite and corundum is thus stabilized. At this pressure, the Al₂O₃ solubility in bridgmanite
275 increases from 6.7 ± 0.5 to 21.7 ± 0.6 mol% with increasing temperature from 1700 to 2500 K. In
276 the same temperature range, the MgSiO₃ solubility in corundum also increases from 16.3 ± 0.8 to
277 38.0 ± 0.5 mol%. Therefore, the two-phase region of bridgmanite and corundum becomes narrower
278 with increasing temperature. The shrinkage of the two-phase region also occurs at higher pressures
279 with increasing temperature. These shrinkages are related to the mixing entropy and enthalpy
280 [[Panero *et al.*, 2006](#)].

281 At a constant temperature, bridgmanite becomes more aluminous with increasing pressure. The
282 Al₂O₃ solubility in bridgmanite increases from 6.7 ± 0.5 to 16 ± 3 mol% with increasing pressure
283 from 27 to 44.5 GPa at 1700 K, from 12.2 ± 0.3 to 21.9 ± 0.6 mol% for pressures from 27 to 42.3
284 GPa at 2000 K, and from 19.2 ± 0.4 to 27.3 ± 0.3 mol% for pressures from 27 to 35 GPa at 2300
285 K. In contrast, the MgSiO₃ content in corundum decreases with increasing pressure, e.g., $16.4 \pm$

286 0.8 to 7 ± 4.0 mol% at 1700 K and 32.2 ± 0.4 to 21.7 ± 0.5 mol% at 2300 K. Both Al_2O_3 and
287 MgSiO_3 enrichment in bridgmanite and corundum, respectively, can be explained by the cation
288 substitution in the crystal structure of bridgmanite and corundum [e.g., [Brodholt, 2000](#); [Kubo and](#)
289 [Akaogi, 2000](#); [Walter *et al.*, 2004](#); [Liu *et al.*, 2016](#)].

290 Increasing proportions of the Al_2O_3 and MgSiO_3 components in bridgmanite and corundum,
291 respectively, increases the lattice parameters of each of the phases (**Figure 7a and 7b**). The lower
292 molar volume of bridgmanite (about 64% of the corundum volume), results in the partitioning of
293 alumina into bridgmanite coexisting with increasingly alumina-rich corundum as pressure
294 increases, accompanied by an increased ratio of bridgmanite to corundum. A simple lever rule
295 analysis of the phase diagram in **Figure 9** rationalizes the variations in phase compositions and
296 proportions as a function of pressure. The opposite situation is seen for the coexisting garnet-
297 corundum assemblage. With bulk system compositions within the two-phase field, the garnet is
298 fixed at the pyrope composition (25 mol% Al_2O_3), and the proportion of garnet decreases with
299 increasing pressure as the MgSiO_3 content of the coexisting corundum increases.

300 The phase boundaries between bridgmanite and two-phase region of bridgmanite and
301 corundum at 2000 and 2300 K, respectively, reported in the present study are close to those
302 obtained using thermodynamics calculation by [Panero *et al.* \[2006\]](#) and prediction by [Irifune and](#)
303 [Tsuchiya \[2007\]](#), respectively, although the rate of the increasing Al_2O_3 content in bridgmanite
304 with increasing pressure in the present study is slightly larger than that in the calculation and
305 prediction. On the contrary, the phase boundary between this two-phase region and corundum is
306 largely different from that obtained in the mentioned calculation and prediction, which may be
307 caused by the poorly constrained thermodynamics parameters of corundum.

308 We note that the compositions of the phases in the recovered samples from experiment runs
309 with the pyropic glass as the starting material are identical to those recovered from experiments
310 for the En₅₀Cor₅₀ oxide mixture within analytical errors, as shown in **Figure 9**. This fact suggests
311 that chemical equilibrium was achieved in our study. This idea is also supported by the identical
312 compositions of two phases obtained from a shorter (5 hours, IRIS 232) and longer (15 hours,
313 IRIS266) heating duration at the same conditions.

314 **4.3 Host phases of Al₂O₃ in the lower mantle**

315 Here, we discuss the Al₂O₃ host phases in the lower mantle at depths between 750 and 1250
316 km, corresponding to pressures of 27 and 50 GPa, respectively. The representative lower-mantle
317 temperatures at these depths are approximately 2000 K [Katsura *et al.*, 2010]. Temperatures in
318 subducted slabs under lower-mantle pressures are unknown, but must be substantially lower than
319 these ambient-mantle temperatures [Kirby *et al.*, 1996].

320 The pyrolite composition contains about 4 wt% of Al₂O₃ [Sun, 1982]. The phase diagram in
321 **Figure 9** suggests that bridgmanite can contain 13 and 29 wt% of Al₂O₃ at a depth of 750 and
322 1250 km, respectively. Therefore, all Al₂O₃ should be accommodated in bridgmanite in the
323 majority of the lower mantle, as already suggested by Irifune [1994]. In subducted slabs, the
324 estimated temperature profile may be at least 300 K lower than the ambient mantle depending on
325 whether the slabs are young or old [Kirby *et al.*, 1996]. At these lower temperatures, the Al₂O₃
326 solubility in bridgmanite is about 7 and 17 wt%, at depth of 750 and 1250 km, respectively.
327 Moreover, the MORB parts of slabs have an Al₂O₃ content up to 16 wt% [Green *et al.*, 1979].
328 Therefore, all Al₂O₃ cannot be fully accommodated in the cold peridotite parts of subducted slabs
329 at 750 km depth, and one additional aluminous phase such as the CF (a MgAl₂O₄ dominated phase

330 with a calcium ferrite-type structure) [Irifune *et al.*, 1991] may therefore form to host the excess
331 Al_2O_3 in this region. At a depth of 1250 km, however, the Al_2O_3 solubility exceeds 16 wt% even
332 at lower temperature, and therefore CF is expected to disappear with increasing subduction depth.

333 Although phase relations in the MgSiO_3 – Al_2O_3 system have been determined as a function of
334 pressure and temperature by our advanced multi-anvil experiments using SD technology and *in*
335 *situ* synchrotron XRD, the chemical systems in the lower mantle and subducted slabs are more
336 complicated. The FeSiO_3 and FeAlO_3 components may change the Al_2O_3 solubility in bridgmanite
337 [e.g., Kesson *et al.*, 1995; Miyajima *et al.*, 1999; Nishio-Hamane *et al.*, 2005]. In particular, the
338 dominance of the FeAlO_3 component in bridgmanite should change the Al_2O_3 solubility relative
339 to that in the MgSiO_3 – Al_2O_3 system [Miyajima *et al.*, 1999; Nishio-Hamane *et al.*, 2005]. The
340 presence of K_2O and Na_2O components would stabilize CF and NAL phases as host phases for the
341 Al_2O_3 component in MORB slabs [e.g., Irifune and Ringwood, 1993; Miyajima *et al.*, 1999, 2001;
342 Ono *et al.*, 2001; Hirose and Fei, 2002; Litasov and Ohtani, 2005], which would decrease the Al_2O_3
343 contents in bridgmanite. Therefore, further studies of phase relations in Fe-, K- and Na-bearing
344 systems are needed to constrain the host phases of Al_2O_3 and their compositions in the lower
345 mantle.

346 4. Conclusion

347 Phase relations in the system MgSiO_3 – Al_2O_3 were determined at pressures between 27 and 45
348 GPa and temperatures of 1700, 2000 and 2300 K. At pressure just below 27 GPa, phase
349 assemblages of garnet+bridgmanite and garnet + corundum are stable for compositions of less and
350 more than 25 mol% Al_2O_3 . At pressures above 27 GPa, another assemblage of bridgmanite and
351 corundum is stabilized for bulk compositions within the two-phase field. The Al_2O_3 and MgSiO_3

352 solubility in bridgmanite and corundum, respectively, increases with increasing temperature.
353 Moreover, bridgmanite becomes more aluminous with increasing pressure and can contain a
354 considerably higher Al_2O_3 component than the pyrope composition. In contrast, the MgSiO_3
355 solubility in corundum decreases with increasing pressure. Additionally, Al_2O_3 incorporation
356 significantly increases the molar volume of bridgmanite, while MgSiO_3 incorporation only slightly
357 increases the volume of corundum. The present study supports the idea that the entire Al_2O_3 content
358 of 4 wt% can be accommodated into bridgmanite in the pyrolitic lower mantle. On the other hand,
359 the Al_2O_3 solubility in bridgmanite is insufficient to accommodate the entire alumina inventory in
360 subducted slabs in the uppermost part of the lower mantle, owing to the low temperatures and
361 limited pressures, and additional Al phases may therefore be present at these conditions.

362

363 **Acknowledgements**

364 We thank T. Kawazoe and D. Druzhbin for their assistances at SPring-8 and D. Krauß for his
365 technical assistance in electron microprobe analysis. We also thank Y. Kojima for his help with
366 the focused ion beam system to prepare TEM sample foils. The manuscript is greatly improved by
367 the constructive comments of R. G. Trønnes and an anonymous reviewer as well as the editorial
368 handling by M. Walter. *In situ* X-ray diffraction measurements were conducted at SPring-8
369 (proposal no. 2015A1359, 2015B1196, 2016A1434, 2016A1172, 2016A1274 and 2016B1094),
370 and some high-pressure cell parts are made in Geodynamics Research Center and supported by
371 PRIUS of Ehime University. All the data are available in the tables and figures in the main text
372 and supporting information. A more detailed discussion of the methodology can be found in the
373 supporting information [Van Cappellen and Doukhan, 1994; Shcheka *et al.* 2006; Tange *et al.*,
374 2009; Liu *et al.*, 2016]. The Focused Ion Beam instrument (FEI, Scios DualBeam) at Bayerisches
375 Geoinstitut was financed by a DFG grant No. INST 91/315-1 FUGG. Z. L. was financially
376 supported by the Bayerisches Geoinstitut Visitor's Program. This study was also supported by
377 research grants to T. K. (BMBF: 05K13WC2, 05K13WC2; DFG: KA3434/3-1, KA3434/7-1,
378 KA3434/8-1, KA3434/9-1).

379

380 **References**

- 381 Akaogi, M., A. Tanaka, and E. Ito (2002), Garnet-ilmenite-perovskite transitions in the system $\text{Mg}_4\text{Si}_4\text{O}_{12}$ –
382 $\text{Mg}_3\text{Al}_2\text{Si}_3\text{O}_{12}$ at high pressures and high temperatures: phase equilibria, calorimetry and implications
383 for mantle structure. *Phys. Earth Planet. Inter.* 132, 303–324.
- 384 Andrault, D., N. Bolfan-Casanova, M. Bouhifd, N. Guignot, and T. Kawamoto (2007), The role of Al-
385 defects on the equation of state of Al-(Mg, Fe)SiO₃ perovskite, *Earth Planet. Sci. Lett.* 263 (3–4), 167–
386 179.
- 387 Brodholt, J. P. (2000), Pressure-induced changes in the compression mechanism of aluminous perovskite
388 in the Earth's mantle, *Nature*, 407, 620–622.
- 389 D'Amour, H., D. Schiferl, W. Denner, H. Schulz, and W. B. Holzapfel (1978), High-pressure single-crystal
390 structure determinations for ruby up to 90 kbar using an automatic diffractometer $P = 0$ kbar. *J. Appl.*
391 *Phys.*, 49, 4411–4416.
- 392 Hirose, K., Y. Fei, T. Yagi, and K. Funakoshi (2001), In situ measurements of the phase transition boundary
393 in $\text{Mg}_3\text{Al}_2\text{Si}_3\text{O}_{12}$: implications for the nature of the seismic discontinuities in the Earth's mantle. *Earth*
394 *Planet. Sci. Lett.* 184, 567–573.
- 395 Hirose, K., and Y. Fei (2002), Subsolvus and melting phase relations of basaltic composition in the
396 uppermost lower mantle. *Geochim. Cosmochim. Acta* 66, 2099–2108.
- 397 Hirsch, L. M., and T. J. Shankland, (1991), Point defects in silicate perovskite. *Geophys. Res. Lett.* 18,
398 1305–1308.
- 399 Fei, Y., Y. Wang, and L. W. Finger (1996), Maximum solubility of FeO in (Mg,Fe)SiO₃ perovskite as a
400 function of temperature at 26 GPa: Implication for the FeO content in the lower mantle. *J. Geophys.*
401 *Res.*, 101, 11525–11530.
- 402 Funamori, N., Yagi, T., Miyajima, N., Fujino, K. (1997), Transformation in garnet: from orthorhombic
403 perovskite to LiNbO₃ phase on release of pressure. *Science* 275, 513–515.
- 404 Irifune, T. (1987), An experimental investigation of the pyroxene-garnet transformation in a pyrolite
405 composition and its bearing on the constitution of the mantle. *Phys. Earth Planet. Inter.* 45, 324–336.
- 406 Irifune, T., K. Fujino, and E. Ohtani (1991), A new high-pressure form of MgAl₂O₄ *Nature* 349, 409–411.

- 407 Irifune, T., and A.E. Ringwood (1993), Phase transformations in subducted oceanic crust and buoyancy
408 relationships at depths of 600–800 km in the mantle. *Earth Planet. Sci. Lett.*, 117, 101–11.
- 409 Irifune, T. (1994), Absence of an aluminous phase in the upper part of the Earth's lower mantle. *Nature*
410 370, 131–133.
- 411 Irifune, T., T. Koizumi, and J. Ando (1996), An experimental study of the garnet-perovskite transformation
412 in the system MgSiO_3 – $\text{Mg}_3\text{Al}_2\text{Si}_3\text{O}_{12}$. *Phys. Earth Planet Inter.* 96, 147–157.
- 413 Irifune, T. and T. Tsuchiya (2007), Phase transition and mineralogy of the lower mantle, in: G.D. Price
414 (Ed.), *Treatise on Geophysics*, vol. 2 Elsevier, pp. 33–62.
- 415 Ishii, T., L. Shi, R. Huang, N. Tsujino, D. Druzhbin, R. Myhill, Y. Li, L. Wang, T. Yamamoto, N. Miyajima,
416 T. Kawazoe, N. Nishiyama, Y. Higo, Y. Tange, and T. Katsura (2016), Generation of pressure over 40
417 GPa using Kawai-type multi-anvil press with tungsten carbide anvils. *Rev. Sci. Instr.* 87, 024501–1–
418 024501–6.
- 419 Ishii, T., R. Sinmyo, T. Komabayashi, T. Boffa-Ballaran, T. Kawazoe, N. Miyajima, K. Hirose and T.
420 Katsura (2017), Synthesis and crystal structure of LiNbO_3 -type $\text{Mg}_3\text{Al}_2\text{Si}_3\text{O}_{12}$: A possible indicator of
421 shock conditions of meteorites, *Am. Min.* 102, 1947–1952.
- 422 Ito, E., and Y. Matsui (1978), Synthesis and crystal-chemical characterization of MgSiO_3 perovskite. *Earth.*
423 *Planet. Sci. Lett.* 38, 443–450.
- 424 Ito, E., A. Kubo, T. Katsura, M. Akaogi, and T. Fujita (1998), High-pressure transformation of pyrope
425 ($\text{Mg}_3\text{Al}_2\text{Si}_3\text{O}_{12}$) in a sintered diamond cubic anvil assembly. *Geophys. Res. Lett.* 25, 821–824.
- 426 Green, D. H., W. O. Hibberson, and A. L. Jaques (1979), Petrogenesis of mid-ocean ridge basalts. In:
427 McElhinny MW (ed.) *The Earth: Its Origin, Structure and Evolution*, pp. 269–299. London: Academic
428 Press.
- 429 Katsura, T., K. Funakoshi, A. Kubo, N. Nshiyama, Y. Tange, Y. Sueda, T. Kubo, and W. Utsumi (2004),
430 A large-volume high-pressure and high-temperature apparatus for in situ X-ray observation, SPEED-
431 Mk.II. *Phys. Earth Planet. Inter.* 143–144, 497–506.
- 432 Katsura, T., A. Yoneda, D. Yamazaki, T. Yoshino, E. Ito (2010), Adiabatic temperature profile in the
433 mantle. *Phys. Earth Planet. Inter.* 183, 212–218.
- 434 Kesson, S. E., J. D. Fitzgerald, J. M. G. Shelley, and R. L. Withers (1995), Phase relations, structure and
435 crystal chemistry of some aluminous perovskites. *Earth Planet. Sci. Lett.* 134, 187–201.

- 436 Keppler, H., and D. J. Frost (2005), Introduction to minerals under extreme conditions. In: R. Miletich
437 (Ed.), *EMU Notes in Mineralogy*, 7, Eötvös University Press, Budapest, pp. 1–30.
- 438 Kirby, S. H., S. Stein, E. A. Okal, and D. C. Rubie (1996), Metastable mantle phase transformations and
439 deep earthquakes in subducting oceanic lithosphere, *Rev. Geophys.* 34, 261–306.
- 440 Kröger, F.A. and H. H. Vink (1956), Relations between the concentrations of imperfections in crystalline
441 solids. *Solid State Phys.* 307–435.
- 442 Kubo, A., and M. Akaogi (2000), Post-garnet transitions in the system $Mg_4Si_4O_{12}$ – $Mg_3Al_2Si_3O_{12}$ up to 28
443 GPa: phase relations of garnet, ilmenite and perovskite. *Phys. Earth Planet Int.* 121, 85–102.
- 444 Liu, Z. D., T. Irifune, M., Nishi, Y. Tange, T. Arimoto, and T. Shinmei (2016), Phase relations in the system
445 $MgSiO_3$ – Al_2O_3 up to 52 GPa and 2000 K. *Phys. Earth Planet Inter.* 257, 18–27.
- 446 Litasov, K. D., and E. Ohtani (2005), Phase relations in hydrous MORB at 18–28 GPa: Implications for
447 heterogeneity of the lower mantle, *Phys. Earth Planet. Inter.* 150, 239–263.
- 448 McCammon, C. A. (1997), Perovskite as a possible sink for ferric iron in the lower mantle. *Nature* 387,
449 694–696.
- 450 McDonough, W. F., and S.-S. Sun (1995), The composition of the Earth, *Chem. Geol.*, 120, 223–253.
- 451 Miyajima, N., K. Fujino, N. Funamori, T. Kondo, and T. Yagi (1999), Garnet-perovskite transformation
452 under conditions of the Earth’s lower mantle: an analytical transmission electron microscopy study.
453 *Phys. Earth Planet. Inter.* 116, 117–131.
- 454 Miyajima, N., T. Yagi, K. Hirose, T. Kondo, K. Fujino, and H. Miura (2001), Potential host phase of
455 aluminium and potassium in the Earth’s lower mantle. *American Mineralogist*, 86, 740–746.
- 456 Navrotsky, A. (1990), A lesson from ceramics. *Science* 284, 1788–1789.
- 457 Navrotsky, A., Schoenitz, M., Kojitani, H., Xu, H., Zhang, J., Weidener, D. J., Jeanloz, R. (2003),
458 Aluminum in magnesium silicate perovskite: formation, structure, and energetics of magnesium-rich
459 defect solid solutions. *J. Geophys. Res.* 108, 2330.

- 460 Nishio-Hamane, D., T. Nagai, K. Fujino, Y. Seto, and N. Takafuji (2005), Fe³⁺ and Al solubilities in
461 MgSiO₃ perovskite: implication of the Fe³⁺AlO₃ substitution in MgSiO₃ perovskite at the lower mantle
462 condition. *Geophys. Res. Lett.*, 32, L16306.
- 463 Ono, S., E. Ito, and T. Katsura (2001), Mineralogy of subducted basaltic crust (MORB) from 25 to 37 GPa,
464 and chemical heterogeneity of the lower mantle. *Earth Planet. Sci. Lett.* 190, 57–63.
- 465 Panero, W. R., S. Akber-Knutson, and L. Stixrude (2006), Al₂O₃ incorporation in MgSiO₃ perovskite and
466 ilmenite. *Earth Planet. Sci. Lett.* 252, 152–161.
- 467 Richmond, N. C., and J. P. Brodholt, (1998) Calculated role of aluminum in the incorporation of ferric iron
468 into magnesium silicate perovskite, *Am. Mineral.* 83, 947–951.
- 469 Ringwood, A. E. (1967), The pyroxene-garnet transformation in the Earth's mantle. *Earth Planet. Sci. Lett.*
470 2, 255–63.
- 471 Ringwood, A. E. (1975), *Composition and Petrology of the Earth's Mantle*. McGraw–Hill, New York.
- 472 Ringwood, A. E. (1991), Phase transformations and their bearing on the constitution and dynamics of the
473 mantle. *Geochim. Cosmochim. Acta*, 55, 2083–2110.
- 474 Shcheka, S. S., M. Wiedenbeck, D. J. Frost, and H. Keppler, (2006), Carbon solubility in mantle minerals.
475 *Earth Planet. Sci. Lett.*, 245, 730–742.
- 476 Stebbins, J. F., S. Kroeker, and D. Andrault, (2001), The mechanism of solution of aluminum oxide in
477 MgSiO₃ perovskite. *Geophys. Res. Lett.* 28, 615–618.
- 478 Sun, S. (1982), Chemical composition and the origin of the Earth's primitive mantle. *Geochimica et*
479 *Cosmochimica Acta* 46, 179–192.
- 480 Tange, Y., T. Irifune, and K. Funakoshi. (2008), Pressure generation to 80 GPa using multianvil apparatus
481 with sintered diamond anvils. *High Pressure Res.*, 28, 245–254.
- 482 Tange, Y., E. Takahashi, Y. Nishihara, K. Funakoshi, and N. Sata (2009), Phase relations in the system
483 MgO–FeO–SiO₂ to 50 GPa and 2000°C: An application of experimental techniques using multianvil
484 apparatus with sintered diamond anvils. *J. Geophys. Res.* 114, B02214.

- 485 Tsuchiya, T. (2003), First-principles prediction of the P–V–T equation of state of gold and the 660–km
486 discontinuity in Earth's mantle. *J. Geophys. Res.* 108, B10.
- 487 Van Cappellen, V., and J. C. Doukhan, (1994), Quantitative transmission X-ray microanalysis of ionic
488 compounds. *Ultramicroscopy*, 53, 343–349.
- 489 Walter, M., A. Kubo, T. Yoshino, J. Brodholt, K. T. Koga, and Y. Ohishi (2004), Phase relations and
490 equation-of-state of aluminous Mg-silicate perovskite and implications for Earth's lower mantle. *Earth
491 Planet. Sci. Lett.* 222, 501–516.
- 492 Walter, M., R. G. Trønnes, L. S. Armstrong, O. Lord, W. A. Caldwell, A. M. Clark (2006), Subsolidus
493 phase relations and perovskite compressibility in the system MgO–AlO_{1.5}–SiO₂ with implications for
494 Earth's lower mantle. *Earth Planet. Sci. Lett.* 248,77–89.
- 495 Weng, K., H. K. Mao, and P. M. Bell (1981), Lattice parameters of the perovskite phase in the system
496 MgSiO₃–CaSiO₃–Al₂O₃. *Carnegie Inst. Washington, Year Book.* 81, 273–277.
- 497 Xu, Y., C. A. McCammon, and B. T. Poe (1998), The effect of alumina on the electrical conductivity of
498 silicate perovskite. *Science*, 282, 922–924.
- 499 Yagi, T., K. Okabe, N. Nishiyama, A. Kubo, and T. Kikegawa (2004), Complicated effects of aluminum
500 on the compressibility of silicate perovskite. *Phys. Earth Planet. Inter.* 143–144, 81–89.
- 501 Zhang, J., and D. J. Weidner (1999), Thermal equation of state of aluminium-enriched silicate perovskite.
502 *Science*, 284, 782–784.

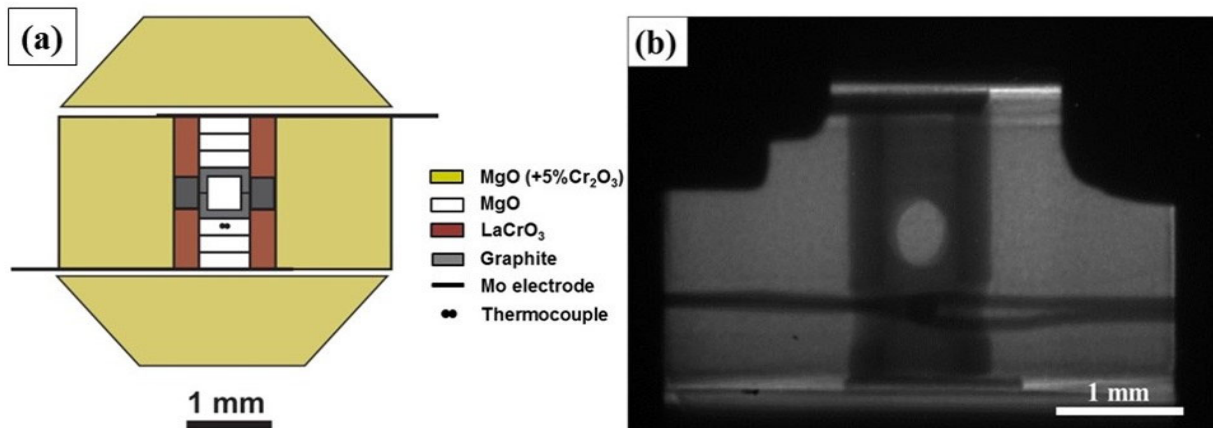
503

504

505

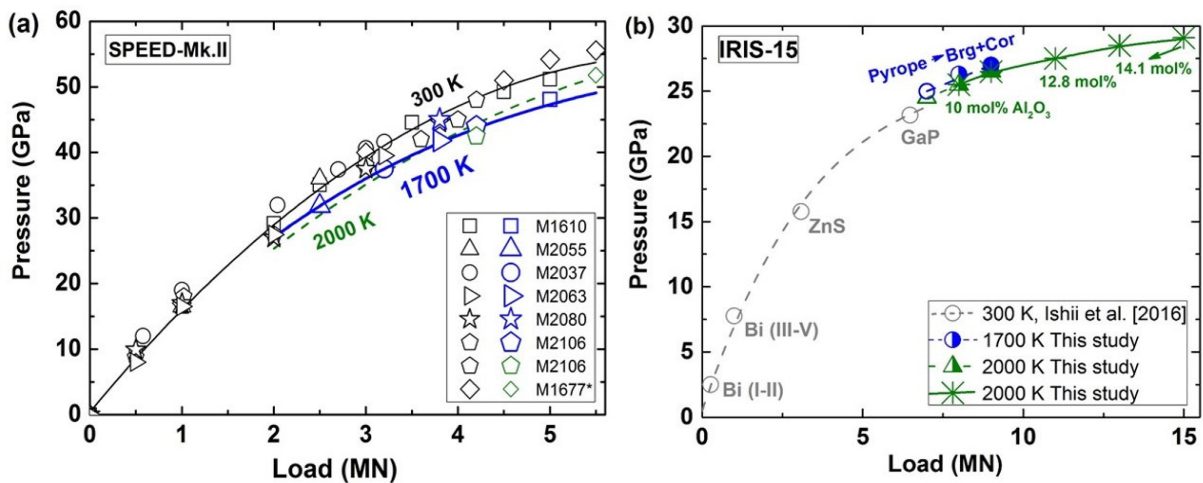
506

507



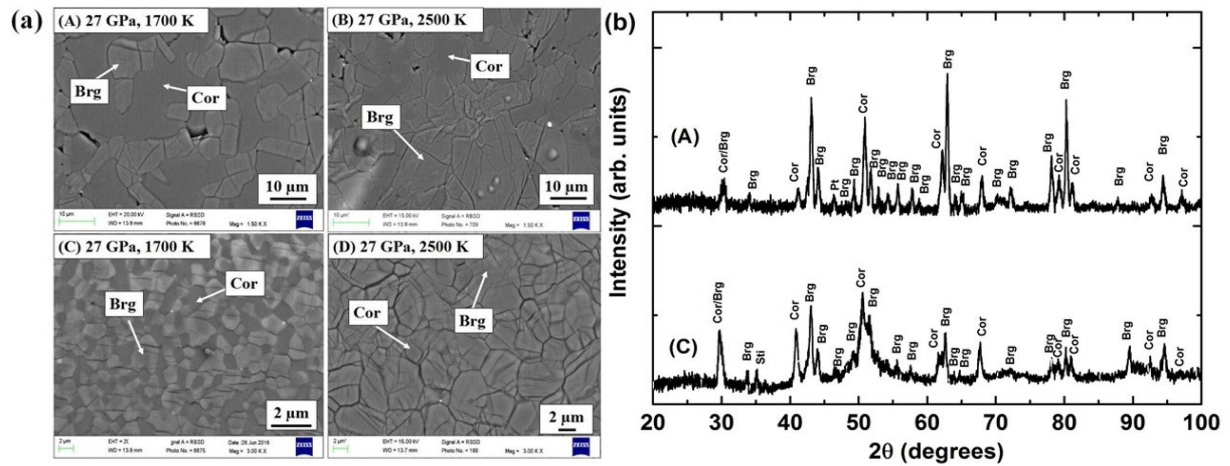
508

509 **Figure 1.** (a) Schematic illustration of the high-pressure cell assembly for *in situ* SD experiments. (b) X-ray radiographic images
 510 of SD cell assembly at ambient conditions. The hot junction of the thermocouple was placed at the bottom of the capsule, and the
 511 diffracted X-ray signals were acquired through the graphite windows.

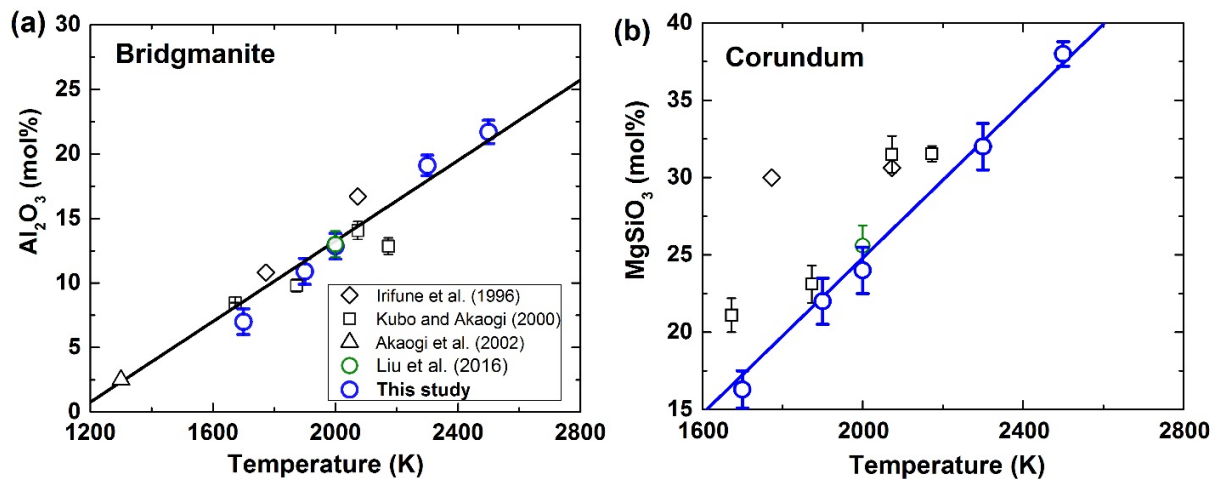


512

513 **Figure 2.** (a) Generated pressure versus the press load at room temperature (300 K, open black symbols), 1700 K (blue symbols, this
 514 study) and 2000 K (green symbols, this study) for *in situ* XRD experiments using a DIA-type apparatus (SPEED-MK.II) at SPring-
 515 8. The black and blue solid lines represent the fitting results of the data at 300 and 1700 K in the present study, and that at 2000 K
 516 together with the symbol of M1677 is from Liu *et al.* [2016]. (b) Pressure calibration curve at 1700 K (circle) and 2000 K (triangle)
 517 for the IRIS-15 multi-anvil apparatus, based on the phase transition of pyrope to bridgmanite and corundum [Hirose *et al.*, 2001]
 518 and various Al₂O₃ solubility (mol%) in bridgmanite at 2000 K [Liu *et al.*, 2016]. Pressure calibration at room temperature condition
 519 is from Ishii *et al.* [2016].



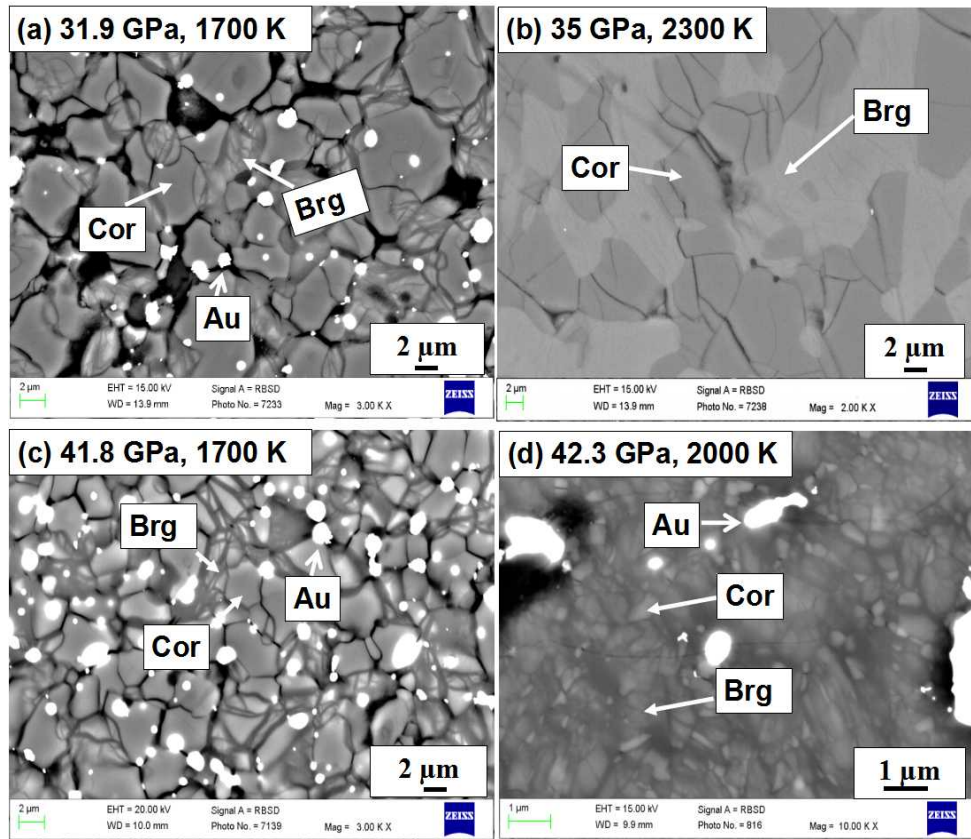
520
 521 **Figure 3.** (a) Representative back-scattered electron images of the run products for En₅₀Cor₅₀ (A-B) and pyropic
 522 compositions (C-D) synthesized at 27 GPa and 1700 and 2500 K, respectively. (b) Selected XRD patterns of the run
 523 products of (A) En₅₀Cor₅₀ and (C) pyropic compositions at 27 GPa and 1700 K, respectively. Abbreviations: Brg,
 524 bridgmanite; Cor, corundum; Sti, stishovite.



525
 526 **Figure 4.** (a) Al₂O₃ solubility in bridgmanite and (b) MgSiO₃ solubility in corundum, respectively, as a function of
 527 temperature at a constant pressure of 27 GPa. The solid black and blue lines are the least-squares fitting of all the data
 528 and only the data in the present study, respectively.

529

530



531

532 **Figure 5.** Selected back-scattered electron images of the run products for $\text{En}_{50}\text{Cor}_{50}$ at 31.9–41.8 GPa and 1700 and
533 2300 K (a–c) and pyropic glass (d) at 42.3 GPa and 2000 K. Abbreviations: Brg, bridgmanite; Cor, corundum; Au:
534 gold.

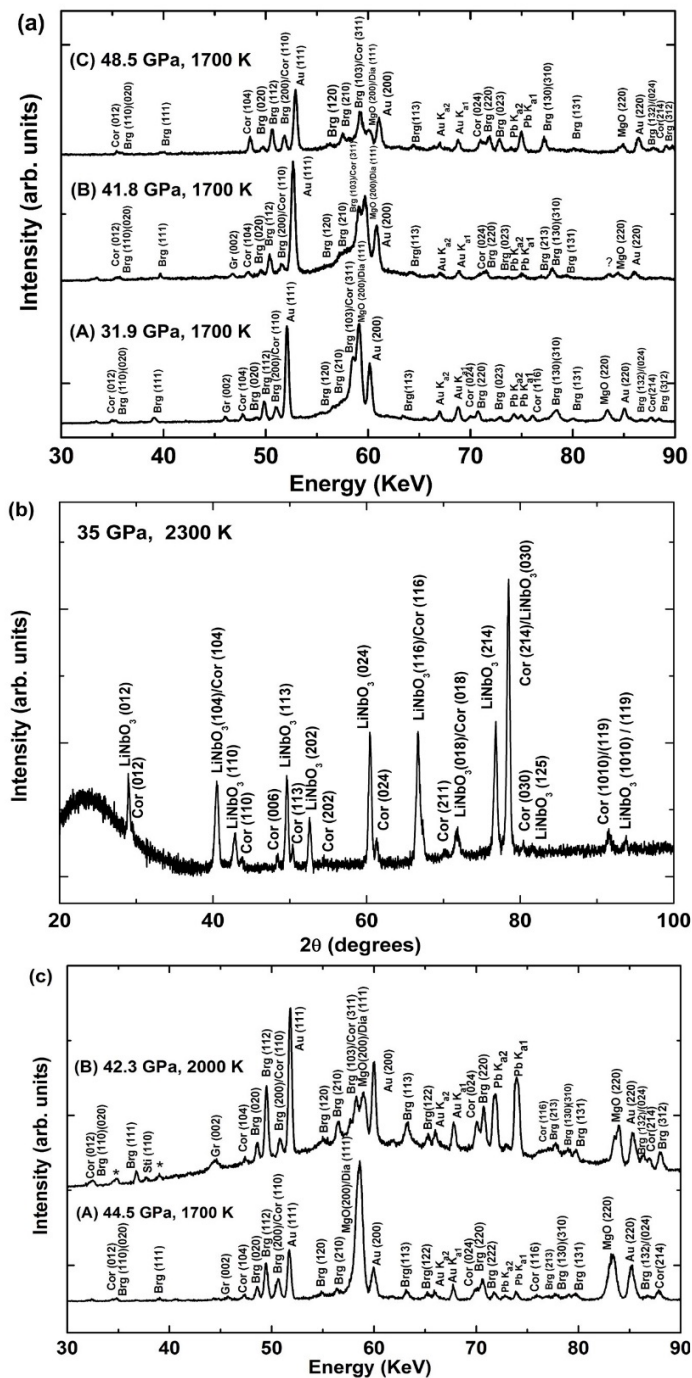
535

536

537

538

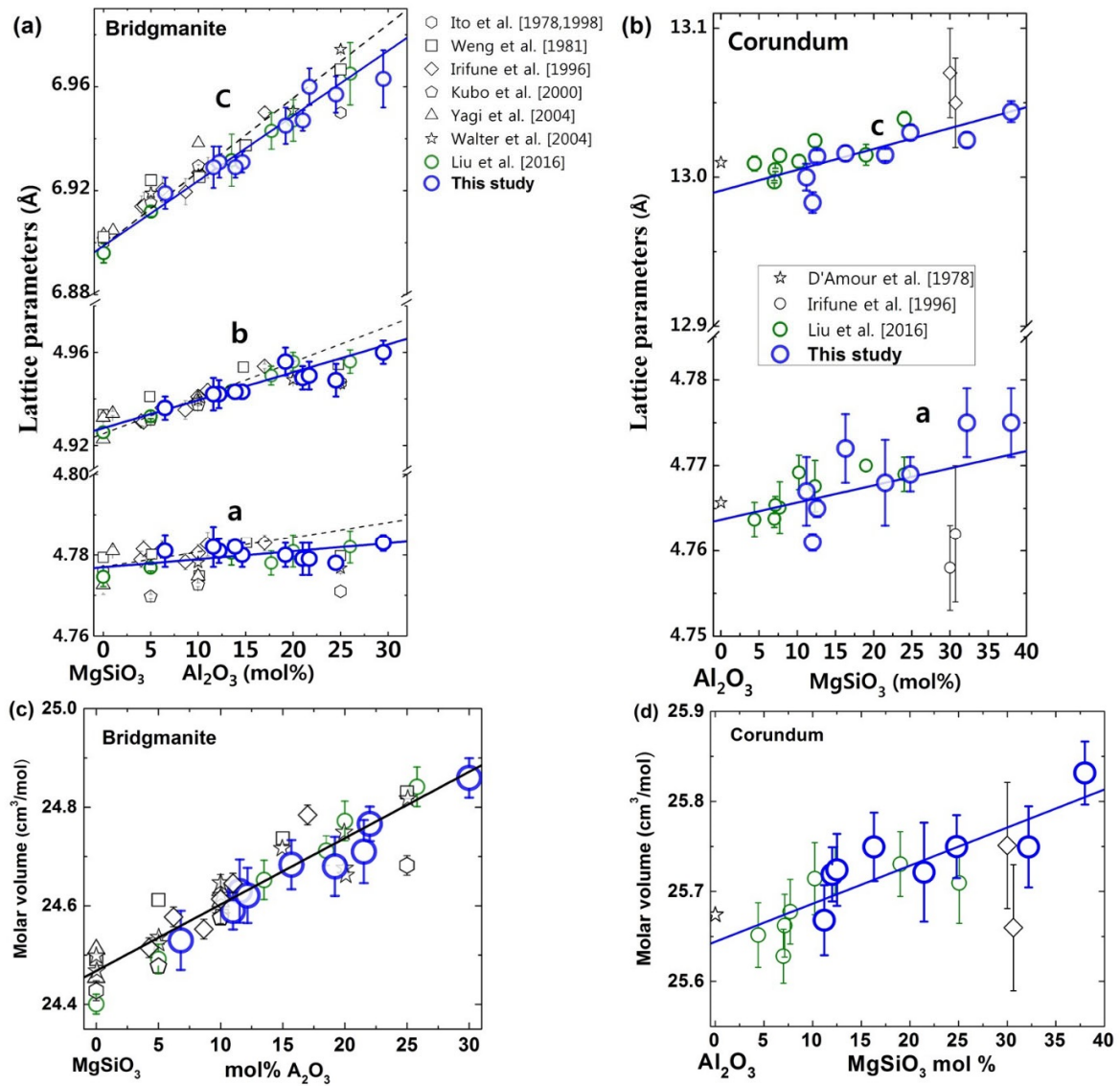
539



540

541 **Figure 6.** Selected (a) *in situ* and (b) quench XRD profiles of $\text{En}_{50}\text{Cor}_{50}$ and (c) *in situ* XRD profiles of the pyropic
 542 glass at various pressure and temperature conditions. Abbreviations: Brg, bridgmanite; Cor, corundum; Dia, diamond;
 543 Sti, stishovite; Gr: graphite. The stars represent the fluorescence of X-ray beam.

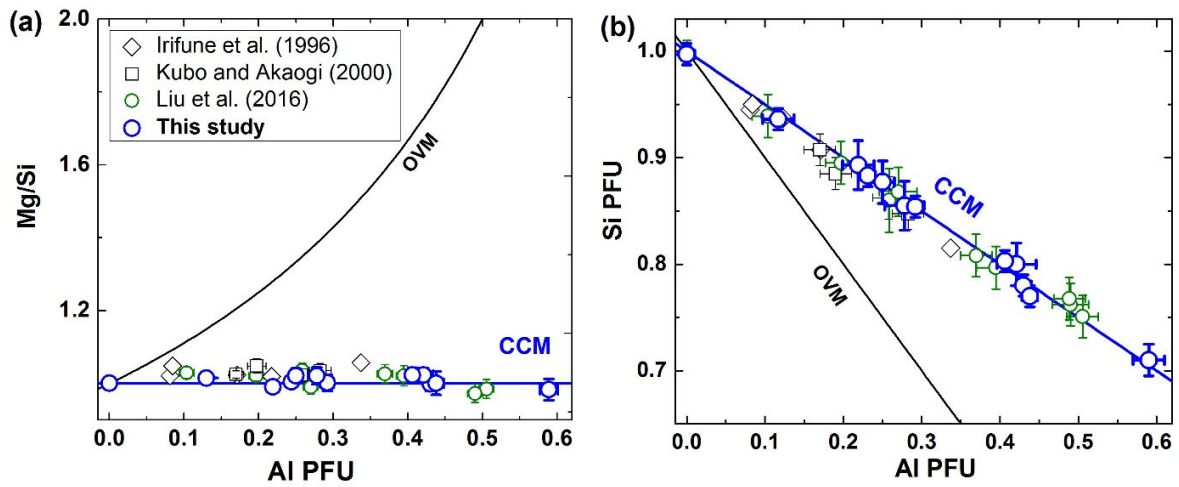
544



545

546 **Figure 7.** Lattice parameter and molar volume of (a and c) bridgmanite and (b and d) corundum versus the Al₂O₃ and
 547 MgSiO₃ content, respectively, in the present and previous work. Solid lines are the linear fitting of the present data
 548 and Liu *et al.* [2016], and the dashed lines are results of Irifune *et al.* [1996].

549



550

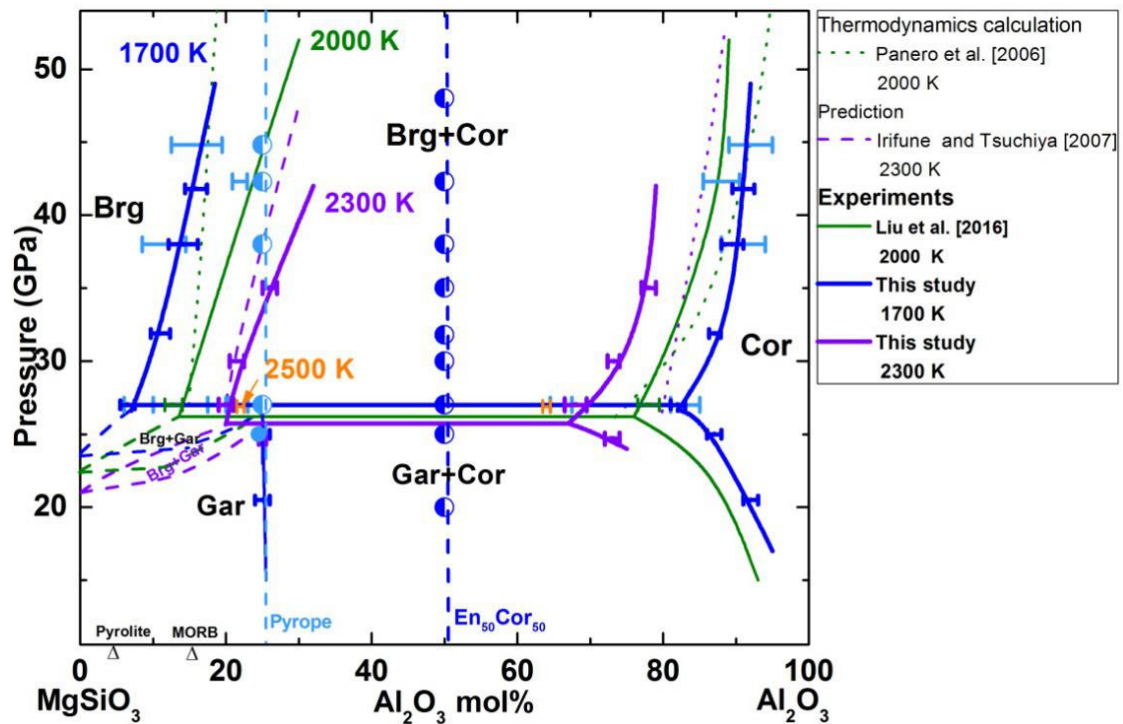
551 **Figure 8.** (a) The ratio between Mg and Si cation and (b) Si cation number versus the Al per formula unit (pfu, based
552 on 3 oxygens) in bridgmanite in the present study and previous works [Irifune *et al.*, 1996; Kubo and Akaogi, 2000;
553 Liu *et al.*, 2016]. Solid blue and black lines indicate the trend expected for trivalent cation incorporation by the charge-
554 coupled substitution mechanism (CCM) and oxygen vacancy substitution mechanism (OVM), respectively.

555

556

557

558



559

560 **Figure 9.** Phase relations in the $\text{MgSiO}_3\text{--Al}_2\text{O}_3$ system at 24–45 GPa and 1700, 2000 and 2300 K in the present and
 561 previous studies. Dark and light blue dashed lines represent the chemical compositions of the starting materials in the
 562 present study. Dark blue circular symbols indicate the high pressure runs using the $\text{En}_{50}\text{Cor}_{50}$ oxide mixture as the
 563 starting material, while light blue circular symbols indicate those for the pyropic glass. The corresponding horizontal-
 564 lined symbols mark the compositions of the coexisting phases for the $\text{En}_{50}\text{Cor}_{50}$ oxide mixture and the pyropic glass.
 565 The phase loop of bridgmanite plus garnet was referenced from Irifune *et al.* [1996], Kubo and Akaogi [2000] and
 566 Irifune and Tsuchiya [2007]. The triangles represent the Al_2O_3 content in the pyrolite and MORB models. Error bars
 567 indicate the uncertainties of chemical compositions. Abbreviations: Brg, bridgmanite; Cor, corundum; Sti, stishovite;
 568 Gar, garnet.

569

570

571

572

573

574 **Table 1** Experimental run conditions and products.

Run no.	Starting sample	Pressure (GPa)	Temperature (K)	Duration (hours)	Phases
S6778	En ₅₀ Cor ₅₀ oxide	20	1700	6	Gar + Cor
S6607	En ₅₀ Cor ₅₀ oxide	25	1700	6	Gar + Cor
	En ₇₅ Cor ₂₅ glass				Gar
S6636	En ₅₀ Cor ₅₀ oxide	24	2300	3	Gar + Cor
IRIS232	En ₅₀ Cor ₅₀ oxide	27	1700	5	Al-Brg + Cor
IRIS266	En ₅₀ Cor ₅₀ oxide	27	1700	15	Al-Brg + Cor
	En ₇₅ Cor ₂₅ glass				Al-Brg + Cor + tr (Sti)
IRIS276	En ₅₀ Cor ₅₀ oxide	27	1900*	2	Al-Brg + Cor
IRIS256	En ₅₀ Cor ₅₀ oxide	27	2000	5	Al-Brg + Cor
	En ₇₅ Cor ₂₅ glass				Al-Brg + Cor
IRIS244	En ₅₀ Cor ₅₀ oxide	27	2300	2	Al-Brg + Cor + tr (Sti)
	En ₇₅ Cor ₂₅ glass				Al-Brg + Cor
IRIS300	En ₅₀ Cor ₅₀ oxide	27	2500*	0.5	Al-Brg + Cor+ tr (Sti)
	En ₇₅ Cor ₂₅ glass				Al-Brg + Cor
IRIS252	En ₅₀ Cor ₅₀ oxide	30	2300	1.5	Al-Brg + Cor
M2055	En ₅₀ Cor ₅₀ oxide	31.9	1700	5	Al-Brg + Cor
S6615	En ₅₀ Cor ₅₀ oxide	35	2300	1.5	Al-Pv + Cor
M2037	En ₅₀ Cor ₅₀ oxide	38.5	1700	5.5	Al-Brg + Cor
M2063	En ₅₀ Cor ₅₀ oxide	41.8	1700	6	Al-Brg + Cor
M2080	En ₇₅ Cor ₂₅ glass	44.8	1700	5	Al-Brg + Cor + tr (Sti)
M2106	En ₇₅ Cor ₂₅ glass	42.3	2000	3	Al-Brg + Cor + tr (Sti)
M1610	En ₅₀ Cor ₅₀ oxide	48.5	1700 ^a	2	Al-Brg + Cor + tr (Sti)
M1677#	En ₅₀ Cor ₅₀ oxide	51.8	2000	3	Al-Brg + Cor

575 * temperature was evaluated from a calibrated power curve derived from the low temperature of 1500 K for IRIS276, and 2400 K for IRIS300.

576 # the run is from Liu et al. [2016].

577 a: temperature is around 1700-1800 K due to the instability of the heater

578 Abbreviations: Gar: garnet, Cor: corundum, Sti: stishovite, Al-Brg: aluminous bridgmanite, Al-Pv: aluminous perovskite; tr: trace.

579

580

581 **Table 2.** Chemical compositions of the coexisting mineral phases in the run products at pressure above 27 GPa

Run no.	Start Comp	Phases	MgO	Al ₂ O ₃	SiO ₂	Total	Mg	Al	Si	Sum
IRIS232	En ₅₀ Cor ₅₀	Brg (n = 15)	37.79 (62)	6.79 (41)	55.33 (78)	99.11 (115)	3.776 (35)	0.521 (35)	3.722 (19)	8.018 (13)
		Cor (n = 12)	6.73 (33)	82.46 (90)	9.19(69)	98.18 (45)	0.671 (35)	6.706 (48)	0.635 (37)	8.012 (19)
IRIS266	En ₅₀ Cor ₅₀	Brg (n = 15)	37.45 (66)	6.93 (36)	55.33 (88)	99.80 (132)	3.754 (26)	0.548 (32)	3.714 (17)	8.014 (19)
		Cor (n = 12)	6.84 (49)	82.07 (27)	9.91(42)	98.82 (70)	0.699 (56)	6.629 (60)	0.679 (26)	8.006 (17)
IRIS256	En ₅₀ Cor ₅₀	Brg (n = 11)	35.67 (26)	12.49 (27)	52.94 (25)	101.10 (63)	3.523 (48)	0.975 (25)	3.507 (14)	8.005 (19)
		Cor (n = 12)	9.74 (29)	74.98 (17)	14.58 (42)	99.05 (57)	0.989 (28)	6.017 (37)	0.993 (24)	7.999 (12)
IRIS276	En ₅₀ Cor ₅₀	Brg (n = 10)	35.36 (27)	11.66 (14)	52.40 (45)	99.42 (81)	3.552 (10)	0.925 (6)	3.530 (7)	8.007 (5)
		Cor (n = 10)	8.61 (37)	79.26 (28)	12.67 (23)	100.54 (46)	0.864 (34)	6.287 (13)	0.853 (17)	8.004 (17)
IRIS244	En ₅₀ Cor ₅₀	Brg (n = 15)	31.50 (54)	20.60 (24)	49.97 (56)	98.79 (93)	3.243 (33)	1.541 (28)	3.222 (14)	8.007 (12)
		Cor (n = 12)	13.08 (17)	67.41 (29)	18.30 (31)	98.80 (19)	1.335 (15)	5.439 (34)	1.253 (19)	8.027 (4)
	En ₇₅ Cor ₂₅	Brg (n = 15)	33.34 (38)	20.04 (35)	49.37 (27)	102.75 (39)	3.243 (33)	1.541 (28)	3.222 (14)	8.007 (12)
		Cor (n = 12)	11.74 (17)	68.73 (39)	17.51 (31)	98.27 (73)	1.203 (12)	5.586 (34)	1.204 (37)	8.000 (14)
IRIS300	En ₅₀ Cor ₅₀	Brg (n = 15)	31.39 (36)	22.38 (52)	47.46 (51)	101.24 (59)	3.100 (31)	1.735 (49)	3.149 (28)	7.984 (11)
		Cor (n = 12)	15.08 (11)	63.14 (83)	23.09 (28)	101.33 (79)	1.497 (7)	4.953 (33)	1.537 (24)	7.987 (8)
	En ₇₅ Cor ₂₅	Brg (n = 15)	31.25 (49)	22.09 (25)	46.97 (31)	100.28 (76)	3.114 (32)	1.740 (18)	3.138 (16)	7.992 (15)
		Cor (n = 12)	14.69 (42)	63.72 (63)	22.10 (128)	100.21	1.474 (26)	5.034 (93)	1.487 (68)	7.996 (18)
IRIS252	En ₅₀ Cor ₅₀	Brg (n = 15)	32.32 (55)	21.66 (69)	47.58 (79)	101.56	3.183 (31)	1.687 (53)	3.143 (31)	8.013 (11)
		Cor (n = 12)	10.97 (30)	72.26 (74)	15.93 (44)	99.16 (26)	1.115 (32)	5.808 (73)	1.086 (31)	8.009 (11)
S6615	En ₅₀ Cor ₅₀	Brg (n = 8)	29.69 (49)	27.76 (23)	42.55 (32)	100#	2.983 (22)	2.197 (17)	2.861 (38)	8.041 (14)
		Cor (n = 10)	8.82 (19)	77.76 (34)	12.44 (25)	99.01 (37)	0.899 (12)	6.277 (25)	0.854 (15)	8.016 (5)
M2055	En ₅₀ Cor ₅₀	Brg (n = 8)	35.26 (27)	11.76 (24)	52.71 (39)	99.73 (58)	3.530 (29)	0.930 (17)	3.538 (21)	7.997 (13)
		Cor (n = 10)	4.75 (51)	87.84 (45)	6.83 (48)	99.42 (81)	0.482 (29)	7.058 (57)	0.465 (29)	8.006 (3)
M2037	En ₅₀ Cor ₅₀	Brg (n = 8)	34.52 (27)	13.72 (40)	51.82 (56)	99.96 (53)	3.414 (17)	1.195 (23)	3.397 (19)	8.005 (12)
		Cor (n = 10)	4.50 (49)	90.10 (53)	6.72 (51)	101.12 (76)	0.450 (36)	7.118 (48)	0.437 (32)	8.004 (5)
M2063	En ₅₀ Cor ₅₀	Brg (n = 5)	34.27 (77)	15.41 (54)	50.95 (90)	101.64 (89)	3.369 (54)	1.275 (22)	3.359 (22)	8.003 (24)
		Cor (n = 11)	3.61 (28)	92.41 (62)	5.23 (22)	101.37 (51)	0.360 (22)	7.283 (34)	0.358 (15)	8.001 (2)
M2106	En ₇₅ Cor ₂₅	Brg (n = 8)	31.55 (69)	22.35 (82)	46.99 (82)	100.89 (98)	3.127 (57)	1.751 (38)	3.124 (47)	8.001 (33)
M1677	En ₅₀ Cor ₅₀	Brg (n = 12)	28.08 (47)	30.00 (64)	42.57 (69)	100.63 (30)	2.789 (58)	2.357 (48)	2.838 (38)	7.984 (27)
		Cor (n = 16)	4.62 (58)	88.98 (80)	6.40 (52)	100.01 (17)	0.467 (6)	7.110 (60)	0.434 (35)	8.010 (23)

582 Oxide analyses are reported in wt%. Cations are reported based on the oxygen number is normalised to 12. Number in parentheses represents
583 standard deviation and is placed in the last digit (s). n: the number of analysis points. #: normalized to 100 due to some amounts (~1 wt%) of WO₃
584 in bridgmanite. Abbreviations: Brg, bridgmanite; Cor, corundum; Comp, composition.